NJC

PAPER

View Article Online
View Journal

Cite this: DOI: 10.1039/c6nj01914e

A new organo-ruthenium substituted tungstotellurate: synthesis, structural characterization and catalytic properties†

Da-Ming Zheng,[a] Rui-Qiang Wang,[a] Yu Du,[a] Guang-Feng Hou,[b] Li-Xin Wu[a] and Li-Hua Bi*[a]

Received (in Montpellier, France)
17th June 2016,
Accepted 25th August 2016

DOI: 10.1039/c6nj01914e

www.rsc.org/njc

Reaction of $[RuC_6H_6Cl_2]_2$ with TeO_2 and $Na_2WO_4{\cdot}2H_2O$ in aqueous solution (pH 4.7) yielded a novel organo-ruthenium supported tungstotellurate polyanion, $[Te_2W_{20}O_{70}(RuC_6H_6)_2]^{8-}$ (**Ru-1**), which is composed of two $[RuC_6H_6]^{2+}$ units linked to a $[Te_2W_{20}O_{70}]^{12-}$ fragment through Ru–O(W) bonds resulting in an assembly with idealized C_{2h} symmetry. Furthermore, the polyanion **Ru-1** was anchored on 3-aminopropyltriethoxysilane (apts)-modified SBA-15 to prepare new catalysts (SBA-15–apts–**Ru-1**) containing different amounts of **Ru-1**, which were characterized using powder X-ray diffraction (XRD), X-ray photoelectron spectroscopy (XPS), N_2-adsorption measurement and Fourier transform infrared reflectance (FT-IR) spectroscopy. Finally, the catalytic activity of SBA-15–apts–**Ru-1** was evaluated for the aerobic oxidation of *n*-tetradecane using air as the oxidant in the absence of any additives or solvents. In addition, the optimum catalytic reaction conditions were also determined.

Introduction

Polyoxometalates (POMs) are an exceptional and distinct family of inorganic metal–oxygen clusters combining remarkable structural variety with intriguing chemical or electronic properties,[1–5] leading to potential applications in various areas including analysis,[6,7] materials science,[8,9] catalysis,[10–13] biomedicine,[14] nanotechnology[15–18] *etc.* As is well-known, POMs have continuously attracted attention for nearly 200 years since the first POM was found in 1826.[19] To date, a large number of novel POMs with various sizes, diverse compositions, and fantastic architectures are still being discovered because of the self-assembly formation mechanism of POMs. Among the synthesis strategies for POMs, the one-pot self-assembly route has become an important method for constructing new POMs up to now.

During the one-pot self-assembly synthesis process, the condensation reactions of different source ions in aqueous media result in the aggregation of octahedral $[MO_6]$ (M = W, Mo, V, Nb, Ta), tetrahedral XO_4 (X = B, Si, Ge, P, As^V) or trigonal pyramidal XO_3 (X = As^{III}, Sb^{III}, Bi^{III}, Se^{IV}, Te^{IV}) building blocks *via* the sharing of corners, edges, and rarely faces, where M is called the addenda atom and X is called the central heteroatom. A literature survey showed that polyoxotungstates containing Te^{IV} as the central heteroatom have been less explored than those containing other central heteroatoms. In 1992, Yurchenko *et al.* revealed the first transition metal-containing tungstotellurates $[M_3(H_2O)_3(\alpha\text{-}Te^{IV}W_9O_{33})_2]^{n-}$ (M = Cu^{2+}, n = 10; M = Fe^{3+}, n = 7), but no single crystal structure was presented.[20] Then, several research groups developed Te^{IV}-based tungstotellurates, synthesized using routine synthetic reactions in aqueous solutions. On the one hand, a series of tungstotellurates without any incorporated transition metals has been reported, for example, $[H_2Te_4W_{20}O_{80}]^{22-}$,[21] $[NaTeW_{15}O_{54}]^{13-}$,[21] $[Te_2W_{17}O_{61}]^{12-}$,[22] $[Te_2W_{16}O_{58}(OH)_2]^{14-}$,[22] $[Te_2W_{18}O_{62}(OH)_2]^{10-}$,[22] $[(WO_2)_4(Te_2W_{15}O_{54})_4]^{32-}$ and $[Te_3W_{21}O_{75}]^{12-}$;[23] on the other hand, different types of transition metal substituted tungstotellurates have been disclosed, for instance, $[Mn_4(H_2O)_{10}(\beta\text{-}TeW_9O_{33})_2]^{8-}$,[24] $[Ni_3(H_2O)_8(WO_2)(TeW_9O_{33})_2]^{8-}$,[25] $[Co_3(H_2O)_8(WO_2)(\beta\text{-}TeW_9O_{33})_2]^{8-}$,[25] $[(V(H_2O)_3)_2(VO_2)(WO_2)(\beta\text{-}TeW_9O_{33})_2]^{6-}$,[25] $[(Zn(H_2O)_3)_2(WO_2)_{1.5}\text{-}(Zn(H_2O)_2)_{0.5}(\beta\text{-}TeW_9O_{33})_2]^{8-}$,[25] $[Cu_3(H_2O)_3(\alpha\text{-}TeW_9O_{33})_2]^{10-}$,[26a] $[Fe_4(H_2O)_2(\beta\text{-}TeW_9O_{33})_2]^{4-}$,[26b] $[\{Ru_4O_6(H_2O)_9\}_2\{Fe(H_2O)_2\}_2(\beta\text{-}TeW_9O_{33})_2H]^{-}$,[26c] $[Pd_3(\alpha\text{-}TeW_9O_{33})_2]^{10-}$,[27] and $[(UO_2)_2(H_2O)_2(\alpha\text{-}TeW_9O_{33})_2]^{12-}$.[28] More recently, Reinoso's group reported two tungstotellurates disubstituted with first-row transition metals and N,O-chelating ligands, $[\{M^{II}(imc)(H_2O)\}_2(WO_2)_2(B\text{-}\beta\text{-}TeW_9O_{33})_2]^{10-}$ (M^{II} = Mn and Co; imc = 1*H*-imidazole-4-carboxylate).[29] Throughout the above literature, it can be found that the number of

[a] College of Chemistry, State Key Laboratory of Supramolecular Structure and Materials, Jilin University, Changchun 130012, P. R. China. E-mail: blhytyyz@163.com
[b] Key Laboratory of Functional Inorganic Material Chemistry (MOE), School of Chemistry and Materials Science, Heilongjiang University, Harbin 150080, P. R. China

† Electronic supplementary information (ESI) available: IR spectra of SBA-15, apts and SBA-15-apts; TGA curve of **Ru-2**. Selected bond distances (Å) for **Ru-2**. CCDC 1471318. For ESI and crystallographic data in CIF or other electronic format see DOI: 10.1039/c6nj01914e

transition metal-containing tungstotellurates synthesized using conventional synthesis methods is still scarce, and the most substituted ions are from the first-row transition metals. Strikingly, tungstotellurates containing second or third-row transition metals have been mentioned rarely in the literature. Therefore, the synthesis and structural characterization using single crystal X-ray diffraction of novel tungstotellurates substituted with second or third-row transition metals is still a great challenge and there are opportunities to discover not only their structures but also their further applications as catalysts.

Here, we report the synthesis and structural characterization of a novel di-organo-ruthenium-grafted tungstotellurate, $Na_6(TMA)_2[Te_2W_{20}O_{70}(RuC_6H_6)_2]\cdot 25H_2O$ (**Ru-2**), which reveals a Krebs' structure with Te^{IV} as the central heteroatom without any disorder. Moreover, we used it as an efficient heterogeneous catalyst toward the aerobic oxidation of *n*-tetradecane under completely green conditions. The development of novel catalysts with a better catalytic performance for *n*-tetradecane oxidation is being extensively pursued in both industrial and academic research.

Experimental section

Materials

All chemicals were utilized as purchased without any further purification. Purified water was used throughout the experiments. Purified water was prepared by passing it through a RiOs 8 unit followed by use of a Millipore-Q Academic purification system.

Synthesis of $Na_6(TMA)_2[Te_2W_{20}O_{70}(RuC_6H_6)_2]\cdot 25H_2O$ (Ru-2)

$Na_2WO_4\cdot 2H_2O$ (0.5 g, 1.5 mmol) was dissolved in 30 mL of distilled water to form solution A, TeO_2 (0.035 g, 0.2 mmol) was dissolved in 10 mL of NaOH (0.25 M) to form solution B; and then solution B was added to solution A dropwise and the mixture was stirred at room temperature for 0.5 h. During this period, the pH of the reaction mixture was adjusted to 4.7 with glacial acetic acid. $[RuC_6H_6Cl_2]_2$ (0.06 g, 0.1 mmol) was added into the mixture, and the solution was heated at 50 °C for 1 h with constant stirring. After cooling to room temperature, the resulting mixture was filtered, followed by addition of 1 mL of a TMA solution (0.1 M) to the filtrate, which was then allowed to evaporate in an open beaker at room temperature. Orange red crystals of **Ru-2** were isolated and collected after approximately two months. Yield: 0.3 g, 48.8% based on Ru. Calcd (found) for **Ru-2**: Na 2.24 (2.22), Ru 3.29 (3.21), Te 4.15 (4.22), W 59.82 (60.24), C 3.91 (3.90), H 1.41 (1.46), N 0.46 (0.49). IR/cm^{-1}: 1489 (m), 1438 (m), 952 (s), 861 (sh), 818 (s), 782 (s), 747 (m), 696 (m), 665 (m), 503 (w), 477 (w).

Preparation of the heterogeneous catalysts SBA-15–apts–Ru-1

The process of surface decoration of the SBA-15 and subsequent fixing of **Ru-1** is described below. Firstly, the mesoporous silica (1 g, SBA-15), purchased commercially, was heated to 130 °C for 6 h in a Schlenk tube under vacuum conditions to remove the adsorbed water, followed by the addition of a solution containing 3-aminopropyltriethoxysilane (apts, 30 μL) and toluene (40 mL) under a nitrogen atmosphere. After refluxing for *ca.* 11 h with stirring, the mixture was filtered and the solid was washed with toluene in order to remove ungrafted apts. Subsequently, the solid was collected and heated at 100 °C for *ca.* 5 h in an oven, and the amino-group decorated mesoporous silica material (SBA-15–apts) was obtained. Secondly, 0.4 g of SBA-15–apts was mixed with 20 mL of water evenly, and then the pH of the mixture was adjusted to *ca.* 2 by adding HCl (2 M). Finally, the protonated silica material was filtered and added to 50 mL of an aqueous solution containing a known amount of **Ru-2** (10 mg, 20 mg and 40 mg) to prepare the anchored samples with **Ru-1** loadings of 1.5%, 2.2%, and 4.5%, respectively, and this was followed by stirring of the mixture for 10 h. Then, the **Ru-1** decorated silica materials were filtered and washed with water several times. The prepared heterogeneous catalysts, SBA-15–apts–**Ru-1**, were dried at 100 °C in an oven.

Characterization

Elemental analysis for C, H and N was performed using a Flash EA1112 analyzer from Thermo Quest Italia SPA. Elemental analysis results for W, Te, Ru and Na were obtained with a Perkin-Elmer Optima 3300 DV ICP-OES Spectrometer. The IR spectra were obtained using a Bruker Vertex 80v spectrometer equipped with a DTGS detector (64 scans), using a dried sample pressed into KBr pellets. Powder X-ray diffraction (XRD) measurements were performed with a Rigaku D/MAX-2500 with Cu Kα radiation and a wavelength of 1.542 Å, operated at 40 kV and 40 mA in Bragg–Brentano geometry. The measurements for the N_2 adsorption isotherms were recorded using a Quantachrome Autosorb-iQ analyzer. The materials were degassed at 150 °C under vacuum for more than 4 h before measurement. The specific surface areas were estimated using Brunauer–Emmett–Teller (BET) means within a P/P_0 range of 0.05–0.35. The distribution of the pore sizes was evaluated using the adsorption branch of the measured isotherms based on the nonlocal density functional theory (NLDFT). The pore volume and pore size were acquired from the adsorption branch of the measured isotherm curves using the NLDFT method. X-ray photoelectron spectroscopy (XPS) spectra were obtained using an ESCALAB-250 spectrometer involving a monochromic X-ray source (Al Kα line, 1486.6 eV). Thermogravimetric analysis (TGA) was accomplished with a TGA Q500 with a heating rate of 10 °C min^{-1} under an air flow.

X-ray crystallography

Data for single-crystal X-ray diffraction of the **Ru-2** compound were collected using an Oxford Diffraction Gemini R Ultra diffractometer with graphite-monochromated Mo Kα radiation (λ = 0.71073 Å) at 293 K. Empirical absorption corrections were applied according to the equivalent reflections. The structure of the **Ru-2** compound was obtained from direct methods, and refined using full-matrix least-squares methods on F^2 (SHELXS-97 crystallographic software package).[30,31] The refinement of all the non-hydrogen atoms was carried out anisotropically. Hydrogen atoms for the benzene and TMA molecules were positioned in calculated places and rode on their parent atoms. The results

Table 1 Crystal data for **Ru-2**

	Ru-2
Empirical formula	$C_{20}H_{86}N_2Na_6O_{95}Ru_2Te_2W_{20}$
Fw	6147.19
Crystal system	Monoclinic
Space group	*C*2/*c*
a (Å)	32.117(2)
b (Å)	13.8184(4)
c (Å)	26.7619(12)
α (deg)	90.00
β (deg)	110.830(6)
γ (deg)	90.00
V (Å^3)	11 100.8(9)
Z	4
D_{calc} (g cm^{-3})	3.678
μ (mm^{-1})	21.537
F(000)	10 872
Reflections collected/unique	31 797/9750
R(int)	0.1093
GOF on F^2	1.061
$R_1{}^a[I > 2\sigma(I)]$	0.0624
$wR_2{}^b[I > 2\sigma(I)]$	0.1294
$R_1{}^a$ (all)	0.0866
$wR_2{}^b$ (all)	0.1450

^{a} $R_1 = \Sigma\|F_o| - |F_c\|/\Sigma|F_o|$. ^{b} $wR_2 = \{\Sigma[w(F_o{}^2 - F_c{}^2)^2/\Sigma w(F_o{}^2)^2]\}^{1/2}$.

including from data collection, the crystal parameters and refinement for **Ru-2** are given in Table 1. Selected bond lengths are shown in Table S1 (ESI†). CCDC 1471318 (for **Ru-2**).

Catalytic experiments

The compound **Ru-2** alone and its immobilized solid SBA-15–apts–**Ru-1** were utilized to detect their heterogeneous catalytic performance for the aerobic oxidation of *n*-tetradecane. A solvent-free aerobic oxidation of *n*-tetradecane was studied using 2 mL of fresh *n*-tetradecane in a 25 mL two-necked-round-bottom flask containing a known amount of undissolved catalyst, without any other additives. The mixtures were heated at different temperatures and stirred under a constant air flow (about 35 mL min^{-1}). After a period of reaction, the resulting mixture was cooled to room temperature, and then a sample was taken out for measurement by GC analysis using a 2014C GC instrument with a flame ionization detector, He as the carrier gas and a HP-FFAP column.

Results and discussion

Characterization of $Na_6(TMA)_2[Te_2W_{20}O_{70}(RuC_6H_6)_2]\cdot 25H_2O$ (Ru-2)

Synthesis. A novel organo-ruthenium $[RuC_6H_6]^{2+}$ disubstituted tungstotellurate polyanion $[Te_2W_{20}O_{70}(RuC_6H_6)_2]^{8-}$ (**Ru-1**) was prepared from a one pot reaction of $[RuC_6H_6Cl_2]_2$ with $Na_2WO_4\cdot 2H_2O$ and TeO_2 in aqueous solution (pH 4.7). On the one hand, this result indicates that the dimeric Ru-precursor $[RuC_6H_6Cl_2]_2$ could be hydrolyzed under such conditions to form a reactive mononuclear electrophile *in situ*; on the other hand, this result further confirms that new POMs could be obtained using the one-pot self-assembly route.

Crystal structure. The structure of **Ru-2** was solved as being in the monoclinic space group *C*2/*c*. The polyanion **Ru-1** of **Ru-2** is composed of two trilacunary B-β-$[TeW_9O_{33}]^{8-}$ Keggin fragments

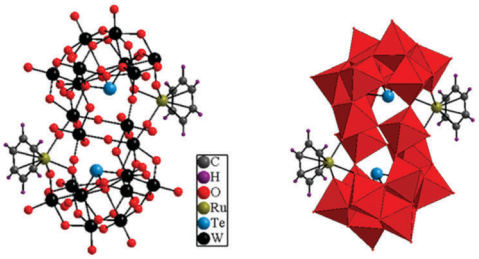

Fig. 1 Ball-and-stick (left) and polyhedral (right) representations of the polyanion $[Te_2W_{20}O_{70}(RuC_6H_6)_2]^{8-}$ (**Ru-1**). The WO_6 octahedra are red.

linked *via* two inner *cis*-WO_2 groups and two outer $[RuC_6H_6]^{2+}$ units leading to a structure with idealized C_{2h} symmetry (see Fig. 1). Alternatively, this polyanion can be described as a dilacunary $[Te_2W_{20}O_{70}]^{12-}$ fragment stabilized by two $[RuC_6H_6]^{2+}$ units. This structural type was just described in 2015 by Reinoso's group for $[\{M^{II}(imc)(H_2O)\}_2(WO_2)_2(B\text{-}\beta\text{-}TeW_9O_{33})_2]^{10-}$ (M^{II} = Mn and Co; imc = 1*H*-imidazole-4-carboxylate),[29] where a little M^{II}//W disorder was observed at the external sites. In contrast, the structure of **Ru-1** doesn't show any disorder at the same sites. Such an observation allows us to conclude that the structure of the dilacunary $[Te_2W_{20}O_{70}]^{12-}$ fragment definitely exists.

This structural type was first reported by Krebs *et al.* for $[X_2W_{22}O_{74}(OH)_2]^{12-}$ (X_2W_{22}) (X = Sb^{III}, Bi^{III}),[32] which is called a Krebs' type compound. Then, a series of first-row transition metal disubstituted Krebs' type compounds were presented.[33] Recently, Proust *et al.* synthesized organo-Ru disubstituted Krebs' compounds through a one pot route, whereas Bi *et al.* prepared the same compounds starting from X_2W_{22}.[34,35] The above results indicate that organo-Ru disubstituted Krebs' compounds can be synthesized using two different routes. We were interested in whether an organo-Ru disubstituted Krebs' compound (X_2W_{22}) with Te^{IV} as the central heteroatom was present. Unfortunately, the Krebs' type polyanion $[Te_2W_{22}O_{74}(OH)_2]^{12-}$ has not been isolated so far. Therefore, we tried to use a one pot procedure to synthesize the target compound. As expected, the organo-Ru disubstituted Krebs' type tungstotellurate polyanion $[Te_2W_{20}O_{70}(RuC_6H_6)_2]^{8-}$ (**Ru-1**) was obtained, and it exhibits a perfect second-row transition metal disubstituted Krebs' type skeleton, compared to $[X_2W_{22}O_{74}(OH)_2]^{12-}$ (X_2W_{22}) (X = Sb^{III}, Bi^{III}) and $[(WO_2)_2M_2(H_2O)_6(\beta\text{-}XW_9O_{33})_2]^{n-}$ (X = Sb^{III}, Bi^{III}; M^{n+} = Mn^{2+}, Fe^{3+}, Co^{2+}, Ni^{2+}, VO^{2+}).[32–37]

Bond valence sum calculations[38] were performed to demonstrate that there are no protonation sites on **Ru-1**, and thereby the charge of the polyanion **Ru-1** must be −8. The negative charge of **Ru-1** in the solid state is balanced by two TMA^+ and six sodium ions, respectively. At same time, elemental analysis was further used to verify the full chemical composition.

Thermogravimetric (TG) analysis. As presented in Fig. S1 (ESI†), the TG curve of the compound **Ru-2** displays two primary weight losses within ranges of about 50–360 and 360–425 °C, in which the first weight loss from 50–360 °C is 8.92% and is attributed to the release of 25 lattice water molecules (calcd 7.32%), and the second weight loss from 360–425 °C is 5.03% and was assigned to the removal of two TMA counter ions and two C_6H_6

ligands coordinated to Ru (calcd 4.95%). Thus, it can be seen that the first weight loss of *ca.* 8.92% was more than 7.32% (the theoretical calculation value), which may be due to loss of some surface water on the sample of **Ru-2** that was not fully dried before the TG analysis. Such behavior has been observed in the TG analysis of other POMs.[39]

Characterization of the heterogeneous catalyst SBA-15–apts–Ru-1

The surface modification process for SBA-15 and the succeeding **Ru-1** immobilization are depicted in Scheme 1. We employed a series of analytical techniques to characterize the heterogeneous catalyst SBA-15–apts–**Ru-1**.

FT-IR spectra. IR spectra of **Ru-2**, SBA-15–apts and SBA-15–apts–**Ru-1** (with **Ru-1** loading of 2.2%) are presented in Fig. 2 (left), where it can be seen that the characteristic vibrational frequencies for **Ru-2** are preserved in SBA-15–apts–**Ru-1**, suggesting that **Ru-1** has been immobilized on SBA-15–apts. Furthermore, as displayed in Fig. 2 (right), it can be observed that the IR spectra of SBA-15–apts–**Ru-1** before and after the catalytic reaction are almost the same, implying that the heterogeneous catalyst SBA-15–apts–**Ru-1** has good stability during the catalytic reaction.

XRD measurements. A series of small angle XRD patterns for the powder state of SBA-15, SBA-15–apts and SBA-15–apts–**Ru-1** with different loadings of **Ru-1** was obtained, as shown in Fig. 3. The following can be observed: (i) all the samples display three characteristic Bragg diffraction peaks, and the intense peak was attributed to a reflection of the (100) plane and two low intensity peaks were assigned to reflections of the (110) and (200) planes for SBA-15. This observation demonstrates that all the samples maintain the well-ordered two-dimensional hexagonal mesoporous structure of SBA-15; (ii) compared to SBA-15 alone, the intensities of the Bragg diffraction peaks decreased with the immobilization of apts and of **Ru-1**, suggesting that apts and subsequently **Ru-1** are fixed inside the channels of SBA-15; (iii) the decrease of the peak intensities with increase of the loading amounts of **Ru-1** further proves that catalysts containing different amounts of **Ru-1** were obtained. In brief, the mesostructure of SBA-15 had been retained after the modification with apts inside the channel surface and the immobilization of **Ru-1** on the surface of SBA-15–apts. Furthermore, we performed N_2 adsorption and desorption experiments to support the above conclusion.

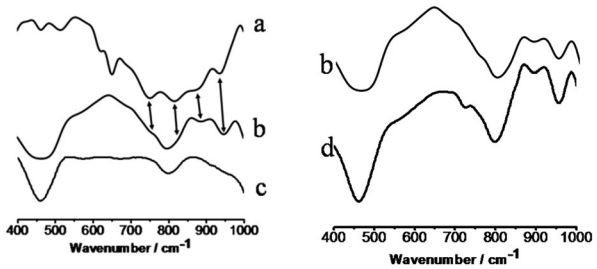

Fig. 2 (left) IR spectra of **Ru-2** (a), SBA-15–apts–**Ru-1** (b) and SBA-15–apts (c); (right) IR spectra of SBA-15–apts–**Ru-1** before (b) and after (d) the catalytic reaction.

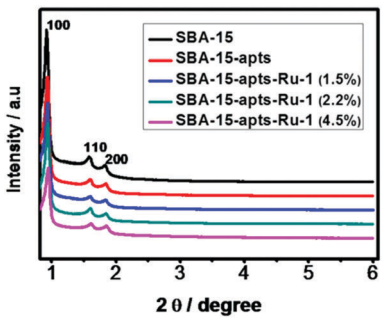

Fig. 3 The low-angle XRD patterns of the samples.

N_2 adsorption/desorption isotherms. Fig. 4 (left) displays N_2 adsorption and desorption isotherms of samples of SBA-15, SBA-15–apts and SBA-15–apts–**Ru-1**. It can be found that: (i) the isotherms of all the samples exhibit nonreversible type IV adsorption curves with a H1 hysteresis loop, which are defined by IUPAC; (ii) each adsorption isotherm shows a sharp inflection in the relative pressure range of 0.50–0.95, indicating capillary condensation inside uniform mesopores; (iii) the absorption amounts are reduced with decreasing pore volume owing to modification with apts and the immobilization of **Ru-1** on SBA-15; (iv) the inflection point for each sample moves to a lower P/P_0, which is ascribed to the decrease of the pore size (see Fig. 4, right).

The Brunauer–Emmett–Teller (BET) method was employed to calculate the surface areas and nonlocal density functional theory (NLDFT) was chosen to assess the pore parameters according to the adsorption branch of the isotherm. Detailed information is

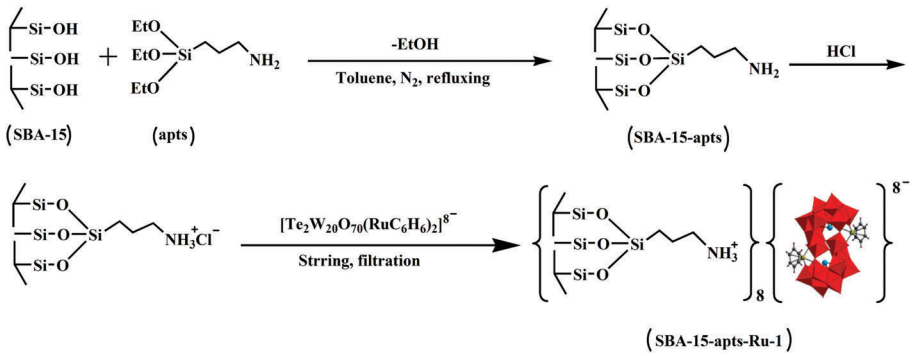

Scheme 1 Synthesis procedure for the heterogeneous catalyst SBA-15–apts–**Ru-1**.

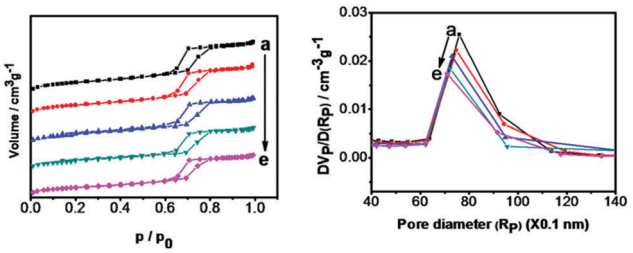

Fig. 4 N_2 adsorption/desorption isotherms (left) and DFT pore size distribution plots (right) of SBA-15 (a), SBA-15–apts (b), SBA-15–apts–**Ru-1** (1.5%) (c), SBA-15–apts–**Ru-1** (2.2%) (d), and SBA-15–apts–**Ru-1** (4.5%) (e).

Table 2 Composition, specific surface area, and pore parameters of SBA-15, SBA-15–apts and SBA-15–apts–**Ru-1** with different loading amounts

Sample (**Ru-1** loading)	Surface area BET [m^2 g]	Pore volume [cc g^{-1}]	Pore diameter [nm]
SBA-15	499	0.87	7.1
SBA-15–apts	488	0.78	7.0
SBA-15–apts–**Ru-1** (1.5%)	379	0.74	6.4
SBA-15–apts–**Ru-1** (2.2%)	360	0.69	6.3
SBA-15–apts–**Ru-1** (4.5%)	353	0.67	6.1

listed in Table 2. It can be found that the pore size, pore volume and surface area decrease after modification with apts and subsequent immobilization of **Ru-1** on SBA-15, demonstrating that the apts and **Ru-1** have been anchored inside the mesochannels of SBA-15. Moreover, the pore size, pore volume and surface area all decrease with an increased loading amount of **Ru-1**, indicating that different amounts of **Ru-1** have been loaded inside the mesochannels of SBA-15. These conclusions are consistent with the XRD patterns.

XPS spectra. We carried out XPS experiments to verify the composition of the as-prepared SBA-15–apts–**Ru-1** heterogenerous catalyst. Fig. 5 shows the characteristic Ru3d, Te3d, W4f, N1s and C1s peaks for SBA-15–apts–**Ru-1**. Components of **Ru-1** and SBA-15–apts exist in the composition of SBA-15–apts–**Ru-1**.

As a result, combining the results of the FT-IR, XRD, and N_2 adsorption and desorption experiments with those of the XPS experiments, it was deduced that the novel polyanion **Ru-1** has been fixed inside the mesochannels of SBA-15 to produce a novel heterogeneous catalyst SBA-15–apts–**Ru-1**.

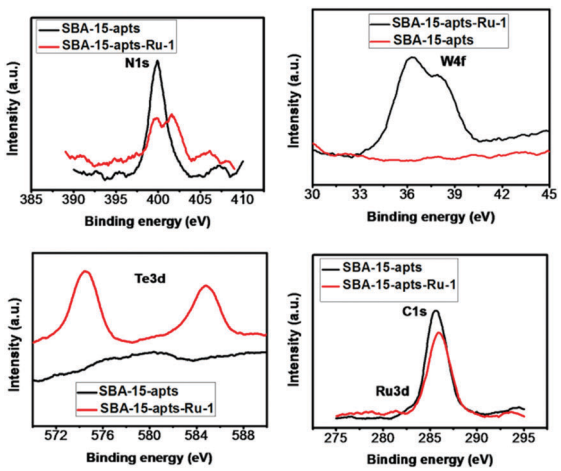

Fig. 5 XPS spectra of SBA-15–apts and SBA-15–apts–**Ru-1**.

Study of the catalytic oxidation reaction of *n*-tetradecane

We chose the catalytic oxidation of *n*-tetradecane to corresponding alcohols and ketones to evaluate the catalytic performance of the catalysts, **Ru-2** alone and SBA-15–apts–**Ru-1**. *N*-Tetradecane includes inert C–H bonds, which make *n*-tetradecane exhibit a lower reactivity in the oxidation reaction. Accordingly, the oxidation of *n*-tetradecane normally requires appropriate solvents, extra additives, sacrificial oxidants and strict control of the experimental conditions such as a high temperature and pressure.[40] To date, very few *n*-tetradecane oxidations have been performed, and a high pressure and temperature were used.[41–43] Therefore, the development of catalysts for *n*-tetradecane oxidation *via* a green reaction process is of paramount importance. The purpose of the present work is to find stable and highly effective catalysts, which can make the *n*-tetradecane oxidation occur under mild experimental conditions with air as the oxidant and without any solvents and additives. Herein, the hybrid compound SBA-15–apts–**Ru-1** is used as a heterogeneous catalyst to investigate the oxidation reaction of *n*-tetradecane under environmentally benign conditions. Our investigation will be dedicated to determining the best catalytic reaction conditions and comparing the catalytic performance of the as-prepared catalyst SBA-15–apts–**Ru-1** under different reaction conditions.

Influence of the loading amount. As is well known, the loading amount of the active constituent on a heterogeneous catalyst will influence its catalytic performance. Thus, we synthesized three heterogeneous catalysts containing different amounts of **Ru-1** (1.5%, 2.2%, 4.5%), which were confirmed using elemental analysis. The catalytic activities of the three catalysts were evaluated. As shown in Fig. 6, we could see that: (i) the heterogeneous catalyst containing 2.2% **Ru-1** was very active, thus this can be considered as the optimal loading of **Ru-1** for the SBA-15–apts–**Ru-1**, which maximizes the catalytic active sites; (ii) compared to the catalytic capacity of **Ru-2** alone (see Table 3), **Ru-1** immobilized on SBA-15 leads to an enhanced catalytic performance and higher turnover frequency. Accordingly, the above comparative study illustrates that the catalytic performance of

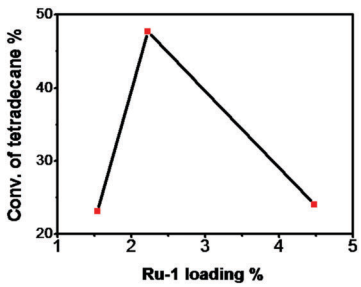

Fig. 6 Conversion of *n*-tetradecane over the catalysts SBA-15–apts–**Ru-1** with different **Ru-1** loadings of 1.5, 2.2 and 4.5%. Reaction conditions: catalyst: 4 mg, *n*-tetradecane: 2 mL, airflow rate: 35 mL min^{-1}, temperature: 150 °C, time: 6 h.

Table 3 Catalytic activity comparison of the catalysts **Ru-2** and SBA-15–apts–**Ru-1** for *n*-tetradecane oxidation with air

Catalyst	POM Loading [%]	Conv. [%]	TOF [h^{-1}]	Product selectivity [%] and distribution	
				Ketones (7-one : 6-one : 5-one : 4-one : 3-one)	Alcohols (7-ol : 6-ol : 5-ol : 4-ol : 3-ol)
Blank	—	9.84	—	52.6	27.7
Ru-2	100	44.01	802	68.8 (20 : 18.2 : 16.4 : 7.3 : 6.9)	16.3 (10.7 : 1.9 : 0.9 : 1.1 : 1.7)
SBA-15–apts–**Ru-1**	2.2	47.90	39 162	61.1 (19.9 : 18.3 : 14.5 : 4.2 : 4.2)	22.2 (5.9 : 4.3 : 2.1 : 4.7 : 5.2)

SBA-15–apts–**Ru-1** definitely depends on the concentration of **Ru-1** in the heterogeneous catalyst.

Determination of the reaction temperature. Based on the results above, the heterogeneous catalyst SBA-15–apts–**Ru-1** with a loading amount of 2.2% was chosen as an example to study the relationship between the catalytic activity and reaction temperature. From Fig. 7, the optimal reaction temperature was determined to be 150 °C, due to the high catalytic activity of the SBA-15–apts–**Ru-1** at this temperature.

Study of the catalyst amount. We selected the catalyst with the optimal loading to investigate the catalytic performance *versus* different catalyst amounts at the optimal reaction temperature. As depicted in Fig. 8, it is clear that the conversion of *n*-tetradecane increases with increase of the catalyst amount, below 4 mg of catalyst, whereas the conversion decreases with increase of the catalyst amount above 4 mg of catalyst. Consequently, the suitable catalyst amount is 4 mg for this catalytic reaction.

Reaction time. We tested the influence of the reaction time on the catalytic performance using the optimized conditions with regards to the loading amount for the catalyst, the temperature of the reaction system and the amount of catalyst. The change trend of the catalytic activity against the reaction time is shown in Fig. 9, which illustrates that the conversion of *n*-tetradecane increases with prolonged reaction time (see Fig. 9 (left)). However, the turnover frequency (TOF) for the *n*-tetradecane conversion reaches a maximum at 6 h, and then decreases (see Fig. 9 (right)), suggesting that the optimal reaction time is 6 h for this catalytic reaction.

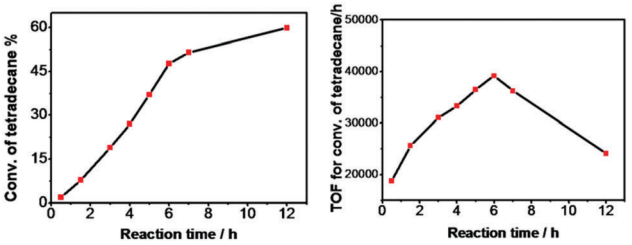

Fig. 9 Conversion (left) and the TOF for conversion (right) of *n*-tetradecane at reaction times of 0.5, 1.5, 3, 4, 5, 6, 7 and 12 h. Reaction conditions: catalyst SBA-15–apts–**Ru-1** with a loading of 2.2%: 4 mg; *n*-tetradecane: 2 mL; airflow rate: 35 mL min^{-1}; temperature: 150 °C.

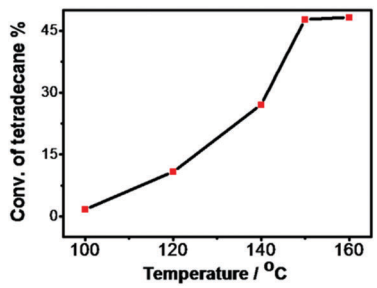

Fig. 7 Conversions of *n*-tetradecane at reaction temperatures of 100, 120, 140, 150 and 160 °C. Reaction conditions: catalyst SBA-15–apts–**Ru-1** with a loading of 2.2%: 4 mg; *n*-tetradecane: 2 mL; airflow rate: 35 mL min^{-1}; time: 6 h.

From the above investigation, it was found that the conversion for *n*-tetradecane oxidation under the optimal catalytic reaction conditions reaches 47.90%. Comparison with the previously reported results to date reveals a better performance of the heterogenerous catalyst SBA-15–apts–**Ru-1** (2.2%) for the solvent free oxidation of *n*-tetradecane.[44]

Reuse and regeneration of the catalyst. With heterogeneous catalysts, a reduction in the catalytic activity is usually encountered owing to leakage of the active species from the surface. Thus, the recyclability of the heterogeneous catalyst SBA-15–apts–**Ru-1** (2.2%) was evaluated *via* five successive cycles of *n*-tetradecane oxidation. The tested heterogeneous catalyst was recovered *via*

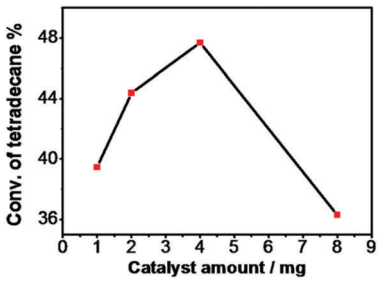

Fig. 8 Conversions of *n*-tetradecane with catalyst amounts of 1, 2, 4 and 8 mg. Reaction conditions: *n*-tetradecane: 2 mL; airflow rate: 35 mL min^{-1}; temperature: 150 °C; time: 6 h; catalyst: SBA-15–apts–**Ru-1** with a loading of 2.2%.

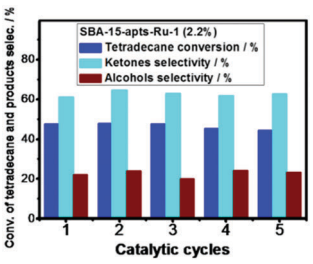

Fig. 10 Evaluation of the recyclability of the SBA-15–apts–**Ru-1** towards the *n*-tetradecane oxidation reaction over five runs. Reaction conditions: catalyst: 4 mg, *n*-tetradecane: 2 mL, airflow rate: 35 mL min^{-1}, temperature: 150 °C, reaction time: 6 h.

filtration, thoroughly washed with distilled water and ethanol, and then dried at 100 °C for *ca.* 5 h after each cycle. As depicted in Fig. 10, no significant change of the *n*-tetradecane conversion occurred after the five cycles, specifically, the catalytic performance of the SBA-15–apts–**Ru-1** was similar to that of the fresh catalyst, implying that the catalyst SBA-15–apts–**Ru-1** could be recycled at least five times without obvious loss of its catalytic activity. Moreover, the selectivity for the ketones and alcohols remained constant, within the range of experimental error, during the five catalytic cycles.

Conclusions

A new organo-Ru grafted tungstotellurate(IV) $Na_6(TMA)_2[Te_2W_{20}O_{70}(RuC_6H_6)_2]\cdot 25H_2O$ (**Ru-2**) was successfully isolated using a one-pot self-assembly synthesis procedure and structurally characterized. Its polyanion $[Te_2W_{20}O_{70}(RuC_6H_6)_2]^{8-}$ (**Ru-1**) consists of two $\{RuC_6H_6\}$ units linked to a $[Te_2W_{20}O_{70}]^{12-}$ fragment *via* three Ru–O(W) bonds, leading to a perfect Krebs' type polyanion (X_2W_{22}) with Te^{IV} as the central heteroatom without any disorder. Furthermore, **Ru-1** was fixed on 3-aminopropyltriethoxysilane (apts)-modified SBA-15 to produce a heterogeneous catalyst, SBA-15–apts–**Ru-1**, with good stability. Characterization of SBA-15–apts–**Ru-1** using FT-IR, XPS, N_2-adsorption and XRD measurements indicated not only that the prepared heterogeneous catalyst retains the hexagonal mesoporous architecture of SBA-15 but also that **Ru-1** was mostly fixed inside the channels of SBA-15. Compared with **Ru-2** alone, the catalyst SBA-15–apts–**Ru-1** revealed an enhanced catalytic performance and improved turnover frequency for the solvent-free aerobic oxidation of *n*-tetradecane under the environmentally-friendly conditions. Furthermore, a series of experiments was carried out to obtain the optimal experimental conditions for the catalytic reaction. Altogether these observations suggest that the catalyst SBA-15–apts–**Ru-1** has potential for application in the solvent-free aerobic catalytic oxidation of *n*-tetradecane.

Acknowledgements

The authors thank the National Natural Science Foundation of China (21173102 and 21473072).

References

1 M. T. Pope, *Polyoxometalates, in Handbook on the Physics and Chemistry of Rare Earths*, Elsevier, Amsterdam, 2008, vol. 38, pp. 337–382.
2 A. Saad, O. Oms, A. Dolbecq, C. Menet, R. Dessapt, H. Serier-Brault, E. Allard, K. Baczko and P. Mialane, *Chem. Commun.*, 2015, **51**, 16088–16091.
3 (*a*) D. D. Zhang, Y. H. Zhang, J. Zhao, P. T. Ma, J. P. Wang and J. Y. Niu, *Eur. J. Inorg. Chem.*, 2013, 1672–1680; (*b*) J. Wang, C. G. Lin, J. Y. Zhang, J. Wei, Y. F. Song and J. B. Guo, *J. Mater. Chem. C*, 2015, **3**, 4179–4187.
4 Y. Matsuki, T. Hoshino, S. Takaku, S. Matsunaga and K. Nomiya, *Inorg. Chem.*, 2015, **54**, 11105–11113.
5 K.Y. Wang, B. S. Bassil, Z. G. Lin, I. Romer, S. Vanhaecht, T. N. Parac-Vogt, C. S. de Pipaon, J. R. Galan-Mascaros, L. Y. Fan and J. Cao, *Chem. – Eur. J.*, 2015, **21**, 18168–18176.
6 J. W. Zuo, N. Gao, Z. G. Yu, L. Kang, K. P. O'Halloran, H. J. Pang, Z. F. Zhang and H. Y. Ma, *J. Electroanal. Chem.*, 2015, **751**, 111–118.
7 (*a*) B. Wang, R. Q. Meng, L. X. Xu, L. X. Wu and L. H. Bi, *Anal. Methods*, 2013, **5**, 885–890; (*b*) B. Wang, R. Q. Meng, L. H. Bi and L. X. Wu, *Dalton Trans.*, 2011, **40**, 5298–5301.
8 J. S. Li, X. J. Sang, W. L. Chen, L. C. Zhang, Z. M. Zhu, T. Y. Ma, Z. M. Su and E. B. Wang, *ACS Appl. Mater. Interfaces*, 2015, **7**, 13714–13721.
9 L. X. Xu, B. Wang, W. M. Gao, L. X. Wu and L. H. Bi, *J. Mater. Chem. C*, 2015, **3**, 1732–1737.
10 H. J. Lv, Y. N. Chi, J. van Leusen, P. Kogerler, Z. Y. Chen, J. Bacsa, Y. V. Geletii, W. W. Guo, T. Q. Lian and C. L. Hill, *Chem. – Eur. J.*, 2015, **21**, 17363–17370.
11 S. S. Wang and G. Y. Yang, *Chem. Rev.*, 2015, **115**, 4893–4962.
12 J. J. Walsh, A. M. Bond, R. J. Forster and T. E. Keyes, *Coord. Chem. Rev.*, 2016, **306**, 217–234.
13 X. Q. Du, Y. Ding, F. Y. Song, B. C. Ma, J. W. Zhao and J. Song, *Chem. Commun.*, 2015, **51**, 13925–13928.
14 A. Saad, W. Zhu, G. Rousseau, P. Mialane, J. Marrot, M. Haouas, F. Taulelle, R. Dessapt, H. Serier-Brault and E. Riviere, *Chem. – Eur. J.*, 2015, **21**, 10537–10547.
15 C. Yvon, A. J. Surman, M. Hutin, J. Alex, B. O. Smith, D. L. Long and L. Cronin, *Angew. Chem., Int. Ed.*, 2014, **53**, 3336–3341.
16 M. T. Pope and U. Kortz, *Polyoxometalates, in Encyclopedia of Inorganic and Bioinorganic Chemistry*, Wiley, Hoboken, 2012.
17 H. N. Kim, T. W. Kim, K. H. Choi, I. Y. Kim, Y. R. Kim and S. J. Hwang, *Chem. – Eur. J.*, 2011, **17**, 9626–9633.
18 S. Q. Liu and Z. Y. Tang, *Nano Today*, 2010, **5**, 267–281.
19 M. T. Pope, *Heteropoly and Isopoly Oxometalates*, Springer, Berlin, 1983.
20 (*a*) E. N. Yurchenko and T. D. Gutsul, *Koord. Khim.*, 1992, **18**, 944–946; (*b*) E. N. Yurchenko, T. D. Gutsul and L. I. Kuznetsova, *Koord. Khim.*, 1992, **18**, 939–943.
21 A. H. Ismail, N. H. Nsouli, M. H. Dickman, J. Knez and U. Kortz, *J. Cluster Sci.*, 2009, **20**, 453–465.
22 C. Ritchie, K. G. Alley and C. Boskovic, *Dalton Trans.*, 2010, **39**, 8872–8874.
23 J. Gao, J. Yan, S. Beeg, D. L. Long and L. Cronin, *Angew. Chem., Int. Ed.*, 2012, **51**, 3373–3376.
24 M. Bösing, A. Nöh, I. Loose and B. Krebs, *J. Am. Chem. Soc.*, 1998, **120**, 7252–7259.
25 E. M. Limanski, D. Drewes, E. Droste, R. Böhner and B. Krebs, *J. Mol. Struct.*, 2003, **656**, 17–25.
26 (*a*) U. Kortz, N. K. Al-Kassem, M. G. Savelieff, N. A. Al Kadi and M Sadakane, *Inorg. Chem.*, 2001, **40**, 4742–4749; (*b*) U. Kortz, M. G. Savelieff, B. S. Bassil, B. Keita and L. Nadjo, *Inorg. Chem.*, 2002, **41**, 783–789; (*c*) I. V. Kalinina, N. V. Izarova and U. Kortz, *Inorg. Chem.*, 2012, **51**, 7442–7444.

27 B. Krebs, M. Droste and M. Piepenbrink, *Polyoxometalate Chemistry: from Topology via Self-Assembly to Applications*, Kluwer, Dordrecht, The Netherlands, 2001, pp. 89–99.
28 A. J. Gaunt, I. May, R. Copping, A. I. Bhatt, D. Collison, O. D. Fox, K. T. Holman and M. T. Pope, *Dalton Trans.*, 2003, 3009–3014.
29 B. Artetxe, S. Reinoso, L. S. Felices, P. Vitoria, A. Pache, J. Martín-Caballero and J. M. Gutiérrez-Zorrilla, *Inorg. Chem.*, 2015, **54**, 241–252.
30 G. M. Sheldrick, *SHELXS-97, Program for solution of crystal structures*, University of Göttingen, Germany, 1997.
31 G. M. Sheldrick, *SHELXL-97, Program for refinement of crystal structures*, University of Göttingen, Germany, 1997.
32 M. Bösing, I. Loose, H. Pohlmann and B. Krebs, *Chem. – Eur. J.*, 1997, **3**, 1232–1237.
33 I. Loose, E. Droste, M. Bösing, H. Pohlmann, M. H. Dickman, C. Rošu, M. T. Pope and B. Krebs, *Inorg. Chem.*, 1999, **38**, 2688–2694.
34 D. Laurencin, R. Villanneau, P. Herson, R. Thouvenot, Y. Jeannin and A. Proust, *Chem. Commun.*, 2005, 5524–5526.
35 L. H. Bi, G. Al-Kadamany, E. V. Chubarova, M. H. Dickman, L. F. Chen, D. S. Gopala, R. M. Richards, B. Keita, L. Nadjo, H. Jaensch, G. Mathys and U. Kortz, *Inorg. Chem.*, 2009, **48**, 10068–10077.
36 (*a*) M. Bösing, A. Nöh, I. Loose and B. Krebs, *J. Am. Chem. Soc.*, 1998, **120**, 7252–7259; (*b*) B. Krebs, E. Droste, M. Piepenbrink and G. C. R. Vollmer, *C. R. Acad. Sci., Ser. IIc: Chim.*, 2000, **3**, 205–210; (*c*) M. Piepenbrink, E. M. Limanski and B. Z. Krebs, *Z. Anorg. Allg. Chem.*, 2002, **628**, 1187–1191.
37 (*a*) L. H. Bi, B. Li and L. X. Wu, *J. Coord. Chem.*, 2009, **62**, 531–539; (*b*) D. Drewes, E. M. Limanski, M. Piepenbrink and B. Z. Krebs, *Z. Anorg. Allg. Chem.*, 2004, **630**, 58–62.
38 I. D. Brown and D. Altermatt, *Acta Crystallogr., Sect. B: Struct. Sci.*, 1985, **41**, 244–247.
39 Y. Wang, X. P. Sun, S. Z. Li, P. T. Ma, J. Y. Niu and J. P. Wang, *Cryst. Growth Des.*, 2015, **15**, 2057–2063.
40 A. Mzé-Ahmed, P. Dagaut, G. Dayma, P. Diévart and K Hadj-Ali, *Combust. Sci. Technol.*, 2014, **86**, 594–606.
41 A. Cavaliere, A. Ciajolo, A. Danna, R. Mercogliano and R. Ragucci, *Combust. Flame*, 1993, **93**, 279–282.
42 A. Ciajolo, A. Danna, R. Barbella and C. Bertoli, *Combust. Sci. Technol.*, 1993, **87**, 127–131.
43 H. P. S. Shen, J. Steinberg, J. Vanderover and M. A. Oehlschlaeger, *Energy Fuels*, 2009, **23**, 2482–2489.
44 R. Q. Wang, L. Suo, D. M. Zheng, Y. Du, L. X. Wu and L. H. Bi, *Inorg. Chim. Acta*, 2016, **443**, 218–223.

